Nanoscale

PAPER

View Article Online
View Journal | View Issue

Check for updates

Cite this: *Nanoscale*, 2025, **17**, 26225

nano-FFA: ink formulation and process optimization in multiphoton 3D laser printing using full factorial analysis

Clara Vazquez-Martel, Samantha O. Catt and Eva Blasco *

Multiphoton 3D laser printing (MPLP) offers a unique combination of sub-micron resolution, geometrical freedom, and property variability. While this technique opens an extensive parameter space to develop new materials, it poses a significant challenge to disentangle and optimize the interrelated effects of chemical composition, process parameters, and resulting material properties. In this context, data analysis through full factorial analysis (FFA) can serve as a crucial tool for the systematic examination of how multiple factors interact and influence the final material properties of 3D printed microstructures, resulting in the identification of key parameters. In this work we propose a three-step approach, called 'nano-FFA', that involves: (1) evaluation of the printability of selected inks *via* scanning electron microscopy (SEM); (2) characterization of 3D printed structures using nanoindentation and vibrational spectroscopy; and (3) identification of interactions between ink formulation and printing parameters *via* FFA. Three scenarios have been investigated using the three-step nano-FFA approach: scenario I focuses on the effect of the photoinitiator concentration. Scenario II examines the influence of different photoinitiator species and scenario III evaluates the effect of the crosslinker. Across all scenarios, a significant interaction is observed between ink composition—*i.e.* photoinitiator concentration, photoinitiator type, and crosslinker—and the laser power (LP) printing parameter. This finding demonstrates that the properties of the final structures can be tailored by precisely selecting these two factors. The results of this study highlight the value of integrating statistical data analysis methods, such as FFA, into 3D printing material optimization toolboxes. Implementation of this new nano-FFA approach can provide a practical method for streamlining ink formulation and process optimization in MPLP, allowing rational ink development over a wide range of applications.

Received 9th July 2025,
Accepted 28th October 2025

DOI: 10.1039/d5nr02899j

rsc.li/nanoscale

Open Access Article. Published on 29 October 2025. Downloaded on 5/13/2026 5:31:44 PM.
This article is licensed under a Creative Commons Attribution 3.0 Unported Licence.

Introduction

Since the early 2000s, the rise of additive manufacturing technologies has fundamentally reshaped how materials are designed, processed, and utilized in engineering and life-science applications.[1] Among these techniques, multiphoton 3D laser printing (MPLP)—also known as direct laser writing—has proven to be a particularly powerful tool due to its ability to create intricate structures with sub-micron resolution.[2–9] A near-infrared (NIR) femtosecond laser is tightly focused inside a suitable photocurable material, a so-called ink, inducing nonlinear multiphoton processes in the focal volume, or 'voxel'. The intensity inside this voxel is high enough to trigger the local curing of the ink, enabling the creation of intricate 3D micro- and nanoscale structures when the laser is scanned within the ink. Controlling the properties of these 3D printed microstructures is critical since it directly conditions potential application. For example, in tissue engineering applications, substrate properties, particularly scaffold stiffness, determines cell fate and tissue development.[10–12] In contrast to the macroscale, accurately characterizing material properties at the micro- and nanoscale presents considerable challenges due to the small size of the samples being studied.[13–15] Overcoming these limitations requires the use of specialized, high-spatial-resolution microscopy-based equipment, such as nanoindentation, as well as spectroscopic methods like Fourier-transform infrared (FTIR) and Raman microspectroscopy.[13,16–22]

Beyond the challenges posed by the nano- and microscale dimensions of MPLP-fabricated structures, material properties are significantly influenced by a complex interplay between the chemical composition of the inks and the printing parameters. In this context, several studies have consistently demonstrated that the mechanical properties of microscale 3D printed materials can be varied by adjusting printing parameters, pre-

Institute of Molecular Systems Engineering and Advanced Materials (IMSEAM), Heidelberg University, Im Neuenheimer Feld 225, 69120 Heidelberg, Germany. E-mail: eva.blasco@uni-heidelberg.de

Open Access Article. Published on 29 October 2025. Downloaded on 5/13/2026 5:31:44 PM. This article is licensed under a Creative Commons Attribution 3.0 Unported Licence.

dominantly the laser power (LP).[13,23–29] There is a positive correlation between LP and the degree of acrylate conversion (DC), which directly affects the stiffness of the 3D printed materials: higher LP generally results in higher DC, with some studies demonstrating a linear relationship.[28] Other processing parameters, such as the scan speed (SS), also influence mechanical properties and printing time. These findings have been observed across various inks, including those that are commercially available (IP-L, IP-Dip, IP-Q, IP-S, and IP-PDMS by Nanoscribe GmbH & Co. KG)[13,23,25,26,28,30–32] and custom-made ones based on acrylate crosslinkers such as pentaerythritol triacrylate (PETA),[27,29] bisphenol A ethoxylate diacrylate (BPAEDA),[29] and poly(ethylene glycol) diacrylate (PEGDA).[24,27,29] Other studies have also explored the effects of different photoinitiators, including 7-diethylamino-3-thenoylcoumarin (DETC), and phenylbis(2,4,6-trimethylbenzoyl) phosphine oxide (BAPO, formerly called Irgacure 819).[29]

Full factorial analysis (FFA), also known as factorial analysis of variance (factorial ANOVA), is a robust statistical method used to compare means across multiple variables with multiple factors (usually denoted by the capital letters A, B, and C). There are some reviews in literature that provide a comprehensive introduction to factorial ANOVA, and how it can be employed to study how these variables can affect the output of an experiment.[33–36] Despite its potential, FFA has not been extensively applied in the field of MPLP. FFA approaches have mainly been used to study the effect of printing parameters (*i.e.* LP and SS) employing commercially available inks.[30–32] When using commercially available inks, control over the exact ink formulation is limited, and therefore, a comprehensive understanding of the links between formulation, printing parameters, and mechanical properties remains challenging. Thus, this work aims to thoroughly examine how the chemical composition of inks interacts with the printing parameters of high-resolution 3D printed microstructures employing FFA. For this purpose, we propose a three-step approach, which we refer to as 'nano-FFA', which includes: (1) assessing the printability of ink formulations based on widely used photoinitiators and crosslinking through scanning electron microscopy (SEM); (2) characterizing 3D printed microstructures through nanoindentation to assess their mechanical properties – specifically the relaxation modulus E_R – and through vibrational spectroscopy (FTIR and Raman) to determine the DC; and (3) revealing the interactions between ink formulation and printing parameters *via* FFA (Fig. 1a). In particular, a 3^k factorial experiment (where $k = 3$) has been employed, meaning three factors with three levels each were evaluated. We have chosen three main factors (Fig. 1b): (A) ink composition, (B) LP, and (C) SS. To optimize the quality of information while maintaining a reasonable level of experimental effort, three 'scenarios' have been designed and systematically examined depending on the factor A of choice, *i.e.* depending on the ink composition (Fig. 1c): the first scenario, scenario I, studied the effects of the photoinitiator concentration. Based on that, in scenario II, the effects of three different photoinitiators were investigated. And lastly, the third scenario, scenario III, explored the effects of three different crosslinkers. This experiment design resulted in a total of 27 different parameter combinations per scenario. By performing a systematic FFA per scenario, a controlled evaluation of the effect of the three main factors was enabled. The results of this study will provide a practical framework for understanding microscale 3D printing, enabling rapid material development tailored to specific applications. This nano-FFA approach is broadly applicable and could be extended to various ink compositions and processing parameters, making it versatile tool in advanced material design.

Results and discussion

The primary objective of this study is to disentangle and optimize the interrelated effects of ink composition, process parameters, and resulting material properties by statistical analysis. For that purpose, three case scenarios were designed (Fig. 1b and c). Inks for MPLP typically consist of a suitable photoinitiator and a crosslinker, along with additives such as solvents to enhance solubility, and absorbers to improve resolution. However, increasing the number of components in an ink formulation complicates the study of interactions between ink composition and processing parameters and makes direct comparisons between inks, and thus printed structures, challenging. To address this point and enable their broader adoption, the inks in this work were intentionally simplified to just two essential components: a crosslinker as the primary constituent and a small amount of photoinitiator to initiate polymerization when irradiated with the laser. Specifically, three commercially available crosslinkers—PETA, BPAEDA, and PEGDA—and three widely used photoinitiators —DETC, (2*E*,6*E*)-2,6-bis (4-(dibutylamino) benzylidene)-4-methylcyclohexanone (BBK), and BAPO—were selected for this study. Regarding factors B and C *i.e.* the printing parameters, LP and SS were varied, with three levels each ('low', 'medium', and 'high') chosen based on the optimal printability window previously determined by SEM. To make comparability more straightforward, the same LPs and SSs were chosen for all ink formulations, as far as possible.

Scenario I: effect of the photoinitiator concentration

First, the effect of the photoinitiator concentration on the final properties of the 3D microprinted structures was systematically investigated. Specifically, the effect of varying DETC concentrations was studied, as it is an efficient and widely used photoinitiator in MPLP.[29,37–41] It is often used in combination with PETA, given its rapid polymerization kinetics and reliability.[29,38,39,41–45] Thus, three PETA-based inks were prepared, containing 0.25 mol%, 0.5 mol% and 0.75 mol% DETC, respectively (Table S1). Then, the printing performance of these three inks was examined (Fig. 2a). To facilitate comparison, tetrahedral structures ($28 \times 28 \times 20$ μm^3) were printed using a broad range of LPs and SSs. The LP was varied from 5 to 45 mW in 2.5 mW increments, and SS was varied from 2 to

 This journal is © The Royal Society of Chemistry 2025

Open Access Article. Published on 29 October 2025. Downloaded on 5/13/2026 5:31:44 PM.
This article is licensed under a Creative Commons Attribution 3.0 Unported Licence.

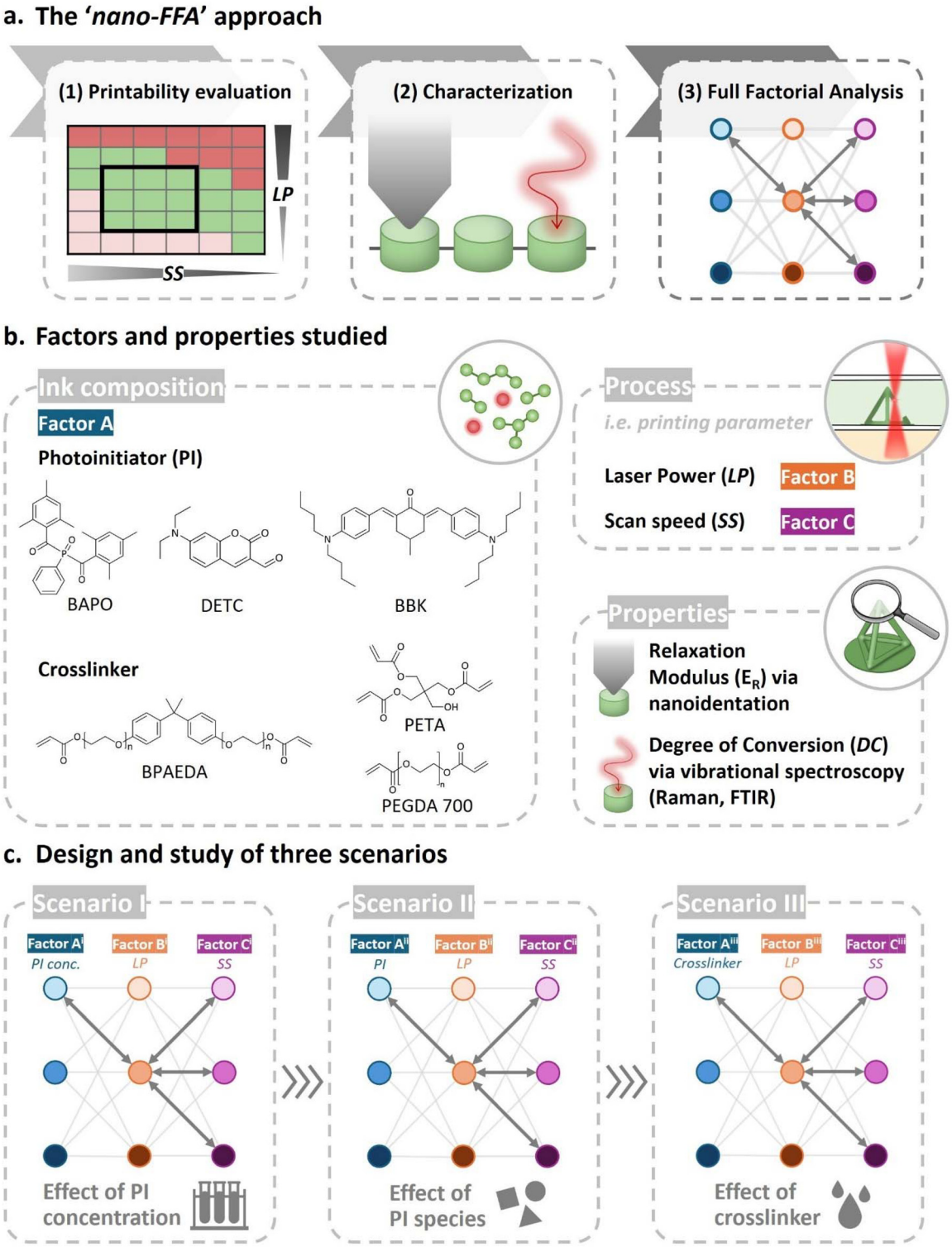

Fig. 1 'nano-FFA' approach to reveal the interactions between ink composition and processing parameter. (a) 'nano-FFA', approach consists of three main steps: (1) the evaluation of the printability of selected inks *via* scanning electron microscopy (SEM); (2) the characterization of 3D printed structures using nanoindentation and vibrational spectroscopy; and (3) the revelation of interactions between ink formulation and printing parameters *via* full factorial analysis (FFA). (b) Overview of the main factors and properties examined in this study: ink composition (factor A) and process parameters, *i.e.* printing parameters laser power (LP, factor B) and scan speed (SS, factor C). (c) Schematic representation the three scenarios of this study following a full factorial ANOVA 3^3 design: I. effect of the photoinitiator (PI) concentration; II. effect of the PI, and III. effect of the crosslinker.

Open Access Article. Published on 29 October 2025. Downloaded on 5/13/2026 5:31:44 PM.
This article is licensed under a Creative Commons Attribution 3.0 Unported Licence.

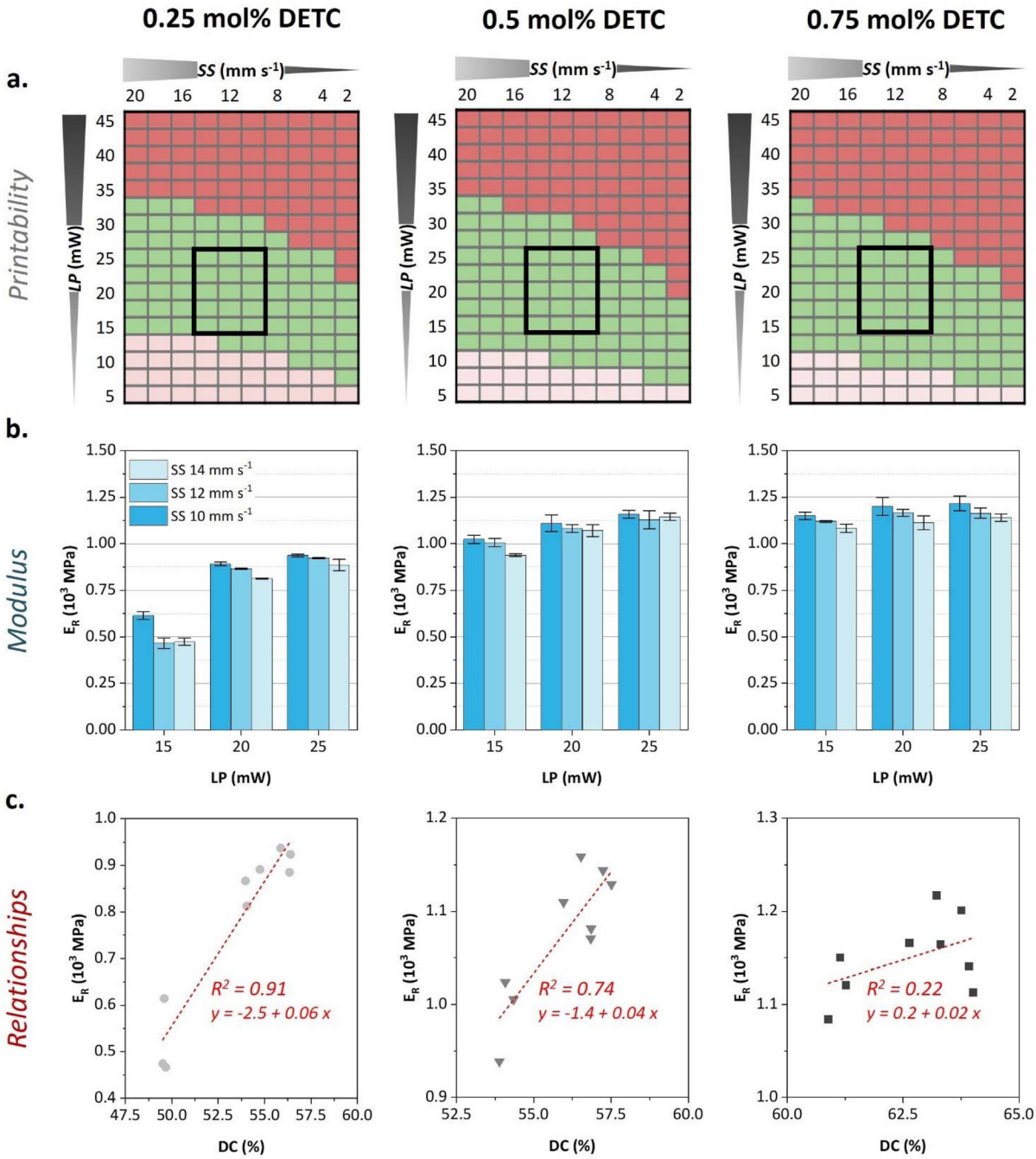

Fig. 2 Scenario I: effect of DETC concentration. (a) Printability for inks with varying DETC concentrations: 0.25 mol% (left), 0.5 mol% (middle), and 0.75 mol% (right) over laser power range from 5 to 45 mW in 2.5 mW increments, and scan speed range from 2 to 20 mm s^{-1} in 2 mm s^{-1} increments. For clarity, the following color coding has been used based on structural quality of the printed structures: Green = successful print; light red = insufficient stability (low energy, undercuring); dark red = explosions and overcuring (high energy). (b) Study of the mechanical properties *via* nanoindentation. All measurements were performed in triplicates, and the results are shown as mean ± SD. (c) Relationship between E_R and DC for different DETC concentrations.

20 mm s^{-1} in 2 mm s^{-1} increments. The structures were imaged with SEM (Fig. S1) to evaluate the quality of resulting tetrahedra and to determine the optimal LP and SS window for successful printing. To illustrate the different printability regions, the SEM images were color coded: When the LP was too low, the tetrahedra collapsed due to insufficient polymerization (light red regions). When the LP was too high, the structures overpolymerized and in some extreme cases 'microexplosions' occurred (dark red regions). As stated in the literature, these instabilities can originate from (1) accumulated exposure

 This journal is © The Royal Society of Chemistry 2025

Open Access Article. Published on 29 October 2025. Downloaded on 5/13/2026 5:31:44 PM. This article is licensed under a Creative Commons Attribution 3.0 Unported Licence.

dose (2) oxygen quenching, and (3) localized heating during microexplosive events.[39,41,46,47] When the LP and SS were in a suitable region, the tetrahedra could be printed successfully, displaying sharp edges and stable overhanging features. These regions are labeled green. The results show that the optimal printability window is broad for all three ink formulations. However, it can be observed that the 'green' window shifts to lower LP and higher SS regions as the concentration of DETC increases.

Once the optimal printability window was determined, three LP levels and three SS levels were selected within these regions to carry out the nanoindentation and vibrational spectroscopy experiments. For this scenario, the chosen printing parameters were compatible across all three ink formulations, due to the similarity of the three inks in composition and printability window, allowing for the selection of the following LP and SS levels (see Fig. 2a, black rectangles): 15, 20, and 25 mW (low, medium, and high LP, respectively), and 10, 12, and 14 mm s^{-1} (low, medium, and high SS, respectively). Then, arrays of cylindrical pillars with 60 μm diameter and 15 μm height were printed using these parameters for further characterization.

In the next step, nanoindentation was used to measure the mechanical properties of the 3D printed pillars across DETC concentrations, LPs, and SSs. The results show that the high LP level (25 mW) yields the highest modulus in all three formulations (Fig. 2b and Fig. S2a). The influence of LP is more pronounced in the case of the ink containing the lowest concentration of DETC (0.25 mol%), with a 53% increase in modulus when increasing LP from 15 mW to 25 mW at constant SS of 10 mm s^{-1} (614 ± 21 MPa *vs.* 937 ± 8 MPa). The effect of SS is also more substantial at the lowest DETC concentration, with a 24% decrease in modulus when increasing the SS from 10 mm s^{-1} to 12 mm s^{-1} or 14 mm s^{-1} (where similar modulus is obtained for both SS). For 0.5 mol% DETC, the effects of LP and SS are less pronounced: the increase in modulus from the lowest to the highest value is 23% at this concentration. For the highest concentration, 0.75 mol%, the changes in modulus are even less pronounced, with just 12% increase from the lowest to the highest value (1084 ± 23 MPa for pillars printed with 15 mW and 14 mm s^{-1} *vs.* 1217 ± 38 MPa for 25 mW and 10 mm s^{-1}). Comparing the three concentrations at the same set of parameters (15 mW and 10 mm s^{-1}), doubling the DETC concentration from 0.25 mol% to 0.5 mol% resulted in a 70% increase in modulus, from 614 ± 21 MPa to 1024 ± 22 MPa. Increasing the DETC concentration further to 0.75 mol%, only increases the modulus by 12%.

To link the mechanical properties with the extent of the network formed during printing, the degree of acrylate conversion (DC) was assessed through FTIR spectroscopy. During 3D printing, the acrylate double bonds are consumed through multiphoton absorption-initiated free radical polymerization. Thus, by comparing the FTIR spectra of the printed pillars with the FTIR spectrum of the 'unprinted' ink, the overall DC can be determined (for more information, please refer to the SI). Similar to E_R, the average DC was found to increase with increasing LP and DETC concentration (Fig. S2b). For 0.25 mol% of DETC, the conversions were relatively low, with approximately 50% acrylate conversion for all pillars printed with 15 mW, regardless of SS. Increasing the LP to 25 mW resulted in an increase in DC, to approximately 56%. 0.75 mol% DETC resulted in the highest conversions, above 60%.

To study the relationship between E_R and DC, linear regression plots have been fitted for each DETC concentration. R^2 values indicate a good linear fit for 0.25 mol% and 0.5 mol% DETC. However, for 0.75 mol% DETC, the R^2 value decreases considerably (Fig. 2c). Nevertheless, a positive correlation was observed between DC and E_R for all DETC concentrations, with pillars having the highest modulus also exhibiting the highest conversion. The highest slope was observed for the lowest DETC concentration (0.25 mol% DETC): At the lowest concentration, the printing parameters, in particular LP, has the highest impact on the properties. These observations may be attributed to the local concentration and diffusivity of the different species such as photoinitiator molecules or oxygen.[41] Thus, inks with higher photoinitiator concentrations become less sensitive to variations in LP and SS (above a certain threshold), resulting in higher DC at comparatively lower LPs. Consequently, E_R is more 'stable' across a broader range of printing parameters.

Scenario II: effect of the photoinitiator

Second, the influence of the photoinitiator on the final properties of 3D printed structures was investigated. To this end, three photoinitiators (DETC, BBK, and BAPO, see Table S5) were selected. The monomer (PETA) was kept constant across all experiments, as was the photoinitiator concentration (0.5 mol%). As introduced in the previous scenario, DETC is a widely used photoinitiator in MPLP. Recent literature has shed light on its initiation mechanism in the presence of PETA:[48] In absence of a co-initiator, DETC undergoes a three photon absorption process, which allows a hydrogen-atom transfer reaction from PETA to DETC, enabling the formation of reactive alkyl radicals that initiate the free radical photopolymerization. In contrast, BBK is a highly sensitive and efficient photoinitiator, also commonly used in combination with PETA.[39,49] Studies have shown that BBK can outperform DETC in terms of printing efficiency.[40,50] Notably, BBK follows a similar activation mechanism as DETC in the absence of co-initators.[51] In contrast, BAPO is typically used as a one-photon absorbing photoinitiator in vat photopolymerization 3D printing.[52] However, its low autofluorescence makes it a popular choice for MPLP as well.[39,53]

As a first step, following the same procedure as in scenario I, the three formulations were used to print the same array of tetrahedral structures over a large range of LPs and SSs and their quality assessed *via* SEM (Fig. 3a and Fig. S3). The results revealed that the optimal printability region for BAPO is relatively narrow, likely due to its lower efficiency compared to DETC and BBK at a concentration of 0.5 mol%. In contrast, BBK demonstrated a significantly broader printability window, allowing for successful printing at very low LP, even as low as 5 mW. However, its high efficiency also made it prone to over-

Open Access Article. Published on 29 October 2025. Downloaded on 5/13/2026 5:31:44 PM.
This article is licensed under a Creative Commons Attribution 3.0 Unported Licence.

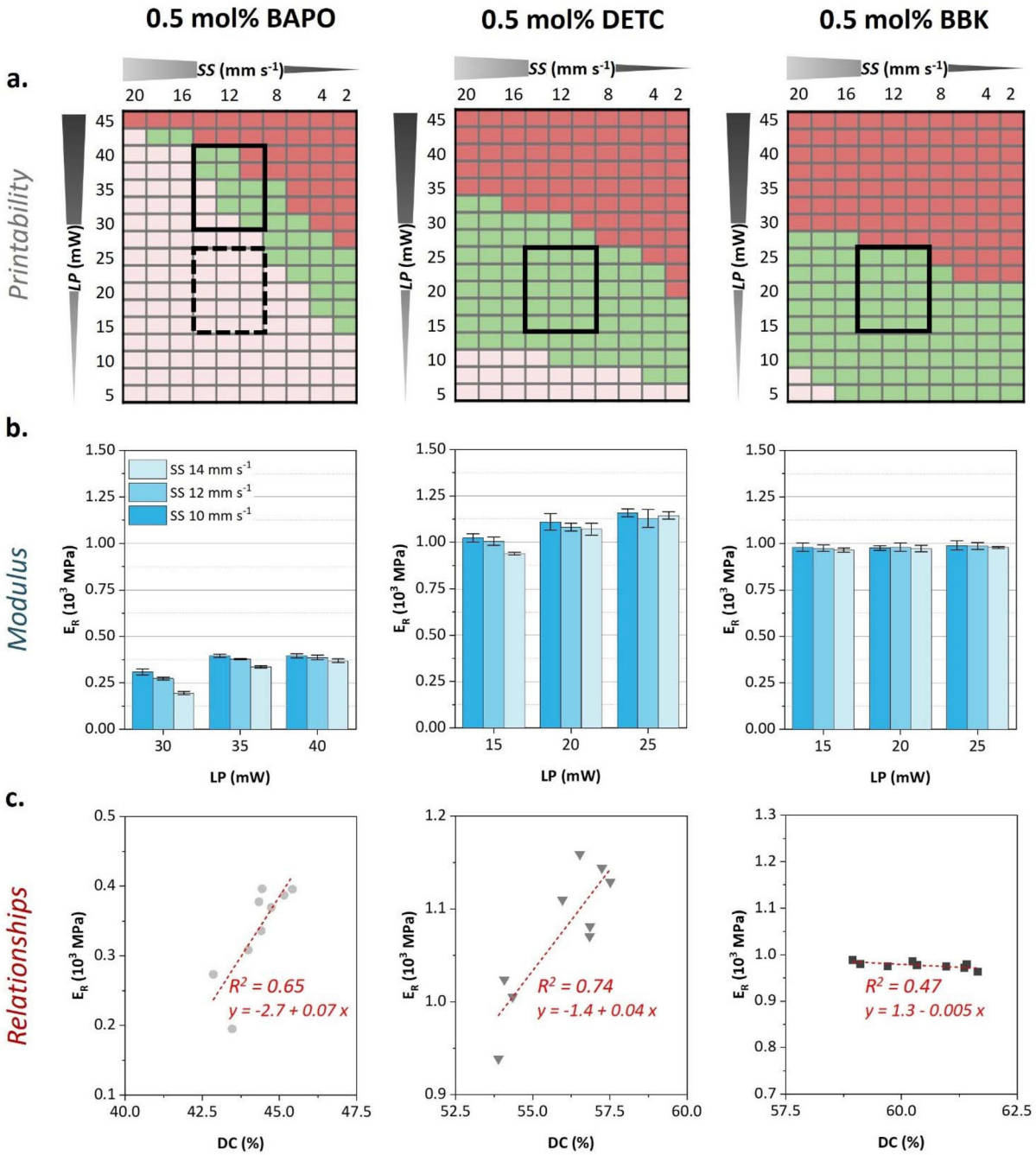

Fig. 3 Scenario II: effect of the photoinitiator. (a) Printability for inks with varying photoinitiators: BAPO (left), DETC (middle), and BBK (right) over laser power range from 5 to 45 mW in 2.5 mW increments, and scan speed range from 2 to 20 mm s^{-1} in 2 mm s^{-1} increments. For clarity, the following color coding has been used based on structural quality of the printed structures: Green = successful print; light red = insufficient stability (low energy, undercuring); dark red = explosions and overcuring (high energy). (b) Study of the mechanical properties *via* nanoindentation. All measurements were performed in triplicates, and the results are shown as mean ± SD. (c) Relationship between E_R and DC for different photoinitiators.

curing. Due to the differing efficiencies of the three photoinitiators, it was challenging to find a single set of LP and SS parameters that were suitable for all three initiators. To reduce the number of parameters changed, the SS was kept constant, thus requiring an increase in LP to reach a suitable printing window for the BAPO ink (see Fig. 3a, black rectangles). Thus, the following LP levels were selected: 15, 20, and 25 mW (low, medium, and high LP, respectively, for DETC/BBK), and 30, 35, and 40 mW (low, medium, and high LP, respectively, for BAPO). As mentioned previously, the SS values remained the same: 10, 12, and 14 mm s^{-1} (low, medium, and high SS, respectively).

 This journal is © The Royal Society of Chemistry 2025

Open Access Article. Published on 29 October 2025. Downloaded on 5/13/2026 5:31:44 PM. This article is licensed under a Creative Commons Attribution 3.0 Unported Licence.

In a next step, using the above-described parameters, arrays of cylindrical pillars with a 60 μm diameter and a height of 15 μm were 3D printed for nanoindentation and vibrational spectroscopy measurements. The results of nanoindentation testing revealed a significant dependence of E_R on the photoinitiator (Fig. 3b and Fig. S4a): despite all formulations being based on PETA, the modulus of BAPO-based materials was substantially lower than that of DETC- and BBK-based ones. For example, at low LP and high SS (30 mW and 14 mm s^{-1}), the modulus of BAPO-based ink was only 195 ± 9 MPa, which is approximately one-fifth of the modulus of DETC-based ink at corresponding conditions (939 ± 8 MPa at 15 mW and 14 mm s^{-1}). As expected, in both BAPO- and DETC-based inks, increasing the LP resulted in a higher modulus. The influence of SS on E_R was most pronounced at low LP levels. For instance, decreasing the SS from high to medium and low (12 mm s^{-1} and 10 mm s^{-1}) in BAPO-based inks, resulted in a 40% and 58% increase of E_R, respectively, with moduli of 273 ± 7 MPa and 309 ± 15 MPa. Overall, the highest modulus measured for inks containing BAPO (396 ± 12 MPa, for 40 mW and 10 mm s^{-1}), was approximately one-third of the highest modulus measured for inks containing DETC (1159 ± 20 MPa, for 25 mW and 10 mm s^{-1}). In contrast, the modulus of BBK-based inks showed relatively little variation across different LP and SS levels. The difference between these values was less than 3%, indicating a relatively consistent modulus across different printing parameters.

The DC was measured *via* FTIR spectroscopy on the same pillars that were previously nanoindented. Similar to E_R, the DC was found to be highly dependent on the photoinitiator of choice (Fig. S4b). The lowest DC was observed for BAPO-based formulations, with conversions ranging from 43% to 45%. This corresponded to the low E_R measured for these ink formulations. The BBK-based formulations exhibited consistently high conversions of approximately 60% across all LPs and SSs screened.

To visualize the relationship between mechanical properties and the degree of conversion, E_R was plotted against DC (Fig. 3c): a positive correlation was observed between DC and E_R for BAPO- and DETC-based inks, with pillars having the highest conversion also exhibiting the highest modulus. The corresponding R^2 values indicated a moderate to good linear fit in these cases. In contrast, the correlation between DC and E_R for BBK-based inks was approximately neutral, with a slope close to zero and a lower R^2: Thus, the obtained E_R for BBK seems to be independent of the processing parameters in the region studied. The underlying mechanisms influencing the performance of photoinitiators for MPLP are very complex and require further fundamental investigation.[40] Differences in the behaviors can be attributed to the different efficiency as well as solubility of the different photoinitiators.[48,51,52] Consequently, BBK generates stable structures at significantly lower LP (5 mW) compared to DETC and BAPO, resulting in higher DCs and more consistent E_R across the processing parameters studied. Thus, the choice of the photoinitiator can affect the mechanical properties of 3D printed microstructures even when the same crosslinker is used.

Scenario III: effect of the crosslinker

Third, to investigate the impact of the crosslinker on the final properties of 3D printed structures, three crosslinkers were screened: PETA, BPAEDA, and PEGDA 700. PETA has an average of three acrylates per molecule and a molecular weight of 298.29 g mol^{-1}. Furthermore, we selected two crosslinkers that have two acrylates per molecule, namely BPAEDA (468.00 g mol^{-1}) and PEGDA 700 (700.00 g mol^{-1}). BPAEDA contains aromatic groups and is therefore more rigid than the flexible PEGDA 700. Thus, despite having the same number of acrylates per molecule, these crosslinkers will produce printed structures with disparate properties. DETC was chosen as the photoinitiator system for this scenario. To ensure a consistent concentration of photoinitiator per reactive moiety of the crosslinker, the DETC concentration was adjusted according to the number of acrylate groups in each crosslinker molecule (Table S9). 0.5 mol% DETC was used for PETA. Thus, for BPAEDA and PEGDA 700, which have 2 acrylate groups per molecule, a lower concentration of 0.33 mol% of DETC was employed. This adjustment maintained a similar molar ratio of photoinitiator to reactive moieties across the different crosslinker systems.

Following the same procedure as in the previous scenarios, tetrahedral structures were printed with the new compositions over a large range of LPs and SSs and their quality was assessed *via* SEM to determine an optimal printability window for each crosslinker (Fig. 4a and Fig. S5). The results showed that the printability performance is highly dependent on the crosslinker, with each exhibiting a unique optimal printability window. BPAEDA had a workable printability window at moderate LPs, PETA displayed a broader one, while PEGDA 700 required higher LPs to achieve optimal printing. These differences are likely due to the interplay of other physical parameters such as viscosity, T_g, and molecular weight, which affect the overall printing kinetics of the inks.[54] As a result, it was challenging to find a single set of LP and SS parameters that worked for all three crosslinkers simultaneously. Similarly as for the BAPO photoinitiator in scenario II, as a compromise, the LP levels for the PEGDA 700-based ink were adjusted to higher values, while maintaining the same SS across all formulations (see Fig. 4a, black rectangles). The following LP levels were selected: 15, 20, and 25 mW (low, medium, and high LP, respectively, for PETA/BPAEDA), 35, 40, and 45 mW (low, medium, and high LP, respectively, for PEGDA 700). As mentioned previously, the SS values remained the same: 10, 12, and 14 mm s^{-1} (low, medium, and high SS, respectively). These parameters were then used to print the samples for nanoindentation and IR measurements.

The results for the mechanical characterization *via* nanoindentation are depicted in Fig. 4b and Fig. S6a. PETA showed the highest E_R values, ranging from 939 ± 8 MPa at 15 mW and 14 mm s^{-1} to 1159 ± 20 MPa at 25 mW and 10 mm s^{-1}. In terms of modulus, BPAEDA follows PETA due to its rigidity despite having only two acrylates per crosslinker molecule. Its E_R values range from moderate to high, spanning from 518 ± 3

Open Access Article. Published on 29 October 2025. Downloaded on 5/13/2026 5:31:44 PM.
This article is licensed under a Creative Commons Attribution 3.0 Unported Licence.

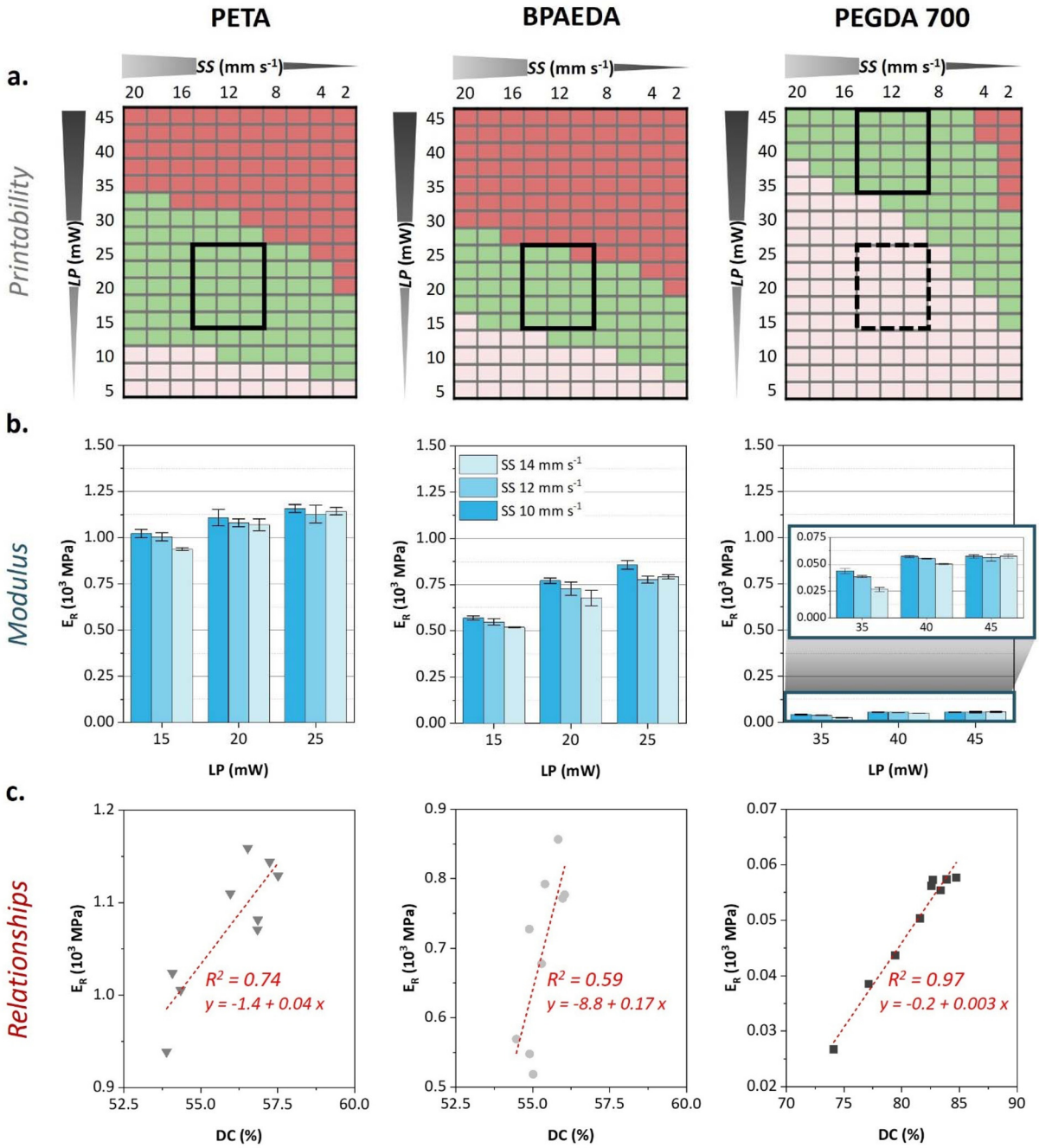

Fig. 4 Scenario III: effect of the crosslinker (a) Printability for inks with varying crosslinkers: PETA (left), BPAEDA (middle), and PEGDA 700 (right) over laser power range from 5 to 45 mW in 2.5 mW increments, and scan speed range from 2 to 20 mm s^{-1} in 2 mm s^{-1} increments. In the case of PETA (3 acrylate groups per molecule) the concentration of DETC was 0.5 mol%. For BPAEDA and PEGDA 700 (2 acrylate groups per molecule) the concentration of DETC was 0.33 mol% to ensure comparability with PETA. For clarity, the following color coding has been used based on structural quality of the printed structures: Green = successful print; light red = insufficient stability (low energy, undercuring); dark red = explosions and overcuring (high energy). (b) Study of the mechanical properties *via* nanoindentation. All measurements were performed in triplicates, and the results are shown as mean ± SD. (c) Relationship between E_R and DC for different crosslinkers.

MPa at 15 mW and 14 mm s^{-1} to 857 ± 24 MPa at 25 mW and 10 mm s^{-1}. As expected, PEGDA 700-based structures showed significantly lower E_R, with 27 ± 2 MPa for low LP and high SS and 57 ± 1 MPa for high LP and low SS, one order of magnitude lower than for the other two crosslinkers.

The DC was measured *via* FTIR spectroscopy for BPAEDA- and PETA-based materials, whereas it was measured *via* Raman spectroscopy for PEGDA 700, due to the softness of the material. Similar to E_R, the DC was found to be highly dependent on the crosslinker (Fig. S6b). BPAEDA-based structures

 This journal is © The Royal Society of Chemistry 2025

Open Access Article. Published on 29 October 2025. Downloaded on 5/13/2026 5:31:44 PM.
This article is licensed under a Creative Commons Attribution 3.0 Unported Licence.

showed relatively consistent DC values, with approximately 55% conversion across different LP and SS conditions. In contrast, PEGDA 700-based structures exhibited the highest DC, ranging from 74% to 85%. Interestingly, despite having the lowest DC values, the structures printed with PETA showed the highest E_R values. This phenomenon has been observed in literature before.[27]

E_R was plotted against DC to study the relationship between mechanical properties and the average degree of conversion for the three crosslinkers (Fig. 4c): A positive correlation was observed, where pillars with the highest conversion also exhibit the highest modulus. The R^2 values indicated a good to excellent linear fit for PETA and PEGDA 700, while the R^2 value for BPAEDA was slightly lower. The 'softer' crosslinkers PEGDA 700 and BPAEDA demonstrate broad tunability of mechanical properties in the studied LP and SS pairs: over 110% for PEGDA 700 and 65% for BPAEDA, when comparing the lowest and the highest measured value of E_R. For PETA, the properties can be varied over 23%. The observed differences between the mechanical property tunability between crosslinkers result from a combination of ink viscosity and molecular architecture, affecting photoinitiator diffusivity and overall ink performance which significantly influences the resulting polymer networks.[41,46,54–57] Thus, crosslinkers such as PEGDA 700 and BPAEDA, which generate less stiff structures than PETA, enable greater tunability of the mechanical properties.

Full factorial analysis and comparison of relevant interaction effects

To disentangle the underlying effects of ink composition, process parameters, and mechanical properties in the three scenarios, we employed a 3^3 replicated full factorial design with 3 replicates per cell. Our focus was on examining the potential interactions between the different factors across scenarios, specifically: the ink composition (DETC concentration in scenario I, photoinitiator in scenario II, and crosslinker in scenario III), and the process parameters (laser power LP and scan speed SS). Given the novelty of the work, we will pursue strong evidence against null hypotheses. Following the guidelines of Benjamin and Berger,[58] we replaced the standard significance threshold $\alpha = 0.05$ with $\alpha = 0.005$. This means that only those interaction effects with a p-value less than 0.005 were considered statistically significant. For a more detailed explanation of the statistical methodology, estimated mean values and confidence intervals please refer to the Experimental section and the SI.

The FFA of scenario I (effect of the photoinitiator concentration) revealed a significant two-way interaction between the DETC concentration and LP ($A^i \times B^i$). The FFA suggests an 'ordinal' interaction (Fig. 5a), which means that the variation in means across the levels of one element either increases or drops when the levels of the other factor change. In this case, the effect of LP on the E_R values is more pronounced for the low DETC concentration, *i.e.* for 0.25 mol% DETC, than the remaining concentration levels (medium and high, *i.e.* 0.5 mol% and 0.75 mol%). In general, the E_R values were higher for high LP levels, *i.e.* 25 mW, and highest when coupled with a high DETC concentration, *i.e.* 0.75 mol% DETC. These results are consistent with previous reports, showing that higher DETC concentrations and LPs result in higher moduli.[29] Overall, the statistical analysis of the experimental results for the mechanical properties suggests that the influence of processing parameters, specifically LP, is more significant with lower concentrations of photoinitiator concentration. The SS was not proven to have a significant interaction effect. In the case of scenario II (effect of the photoinitiator, Fig. 5b) the FFA revealed a significant ordinal two-way interaction between the photoinitiator and LP ($A^{ii} \times B^{ii}$): E_R is highest at a high level of LP (25 mW for DETC and BBK, and 40 mW for BAPO). The differences in E_R values between the three LP levels is larger for DETC and BAPO, but barely present for BBK. Overall, the highest E_R values are obtained for DETC.

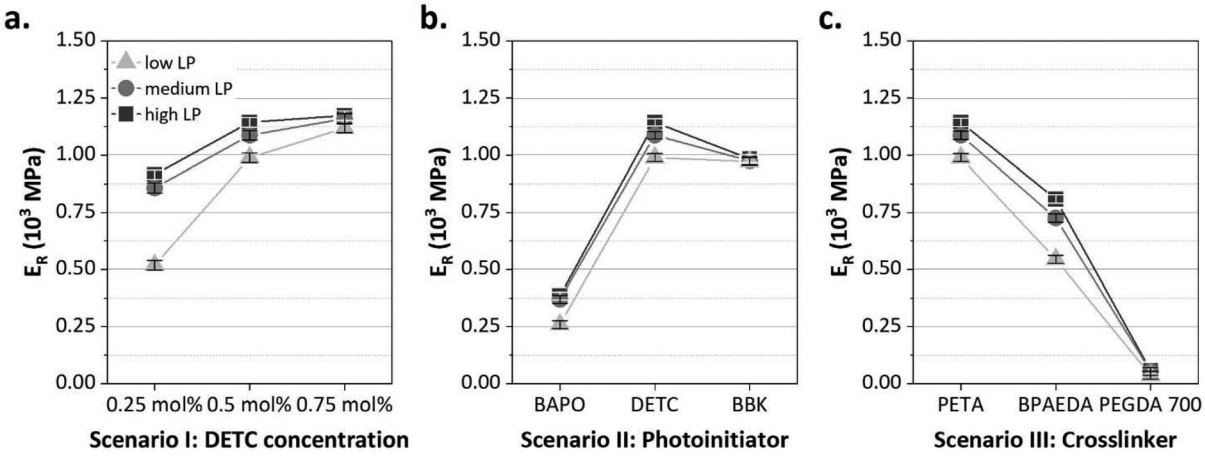

Fig. 5 Two-way interaction plots of the three studied scenarios. (a) Scenario I (effect of the photoinitiator concentration) showed a two-way interaction between the DETC concentration and LP ($A^i \times B^i$). (b) Scenario II demonstrated a two-way interaction between the photoinitiator and LP ($A^{ii} \times B^{ii}$). (c) Scenario III showed a two-way interaction between the crosslinker and LP ($A^{iii} \times B^{iii}$).

Open Access Article. Published on 29 October 2025. Downloaded on 5/13/2026 5:31:44 PM.
This article is licensed under a Creative Commons Attribution 3.0 Unported Licence.

Table 1 Summary of the relevant interaction effects obtained *via* the nano-FFA approach

Scenario	Significative interaction effects
Scenario I	DETC conc. × LP ($A^i \times B^i$)
DETC concentration (A^i)	
Laser power LP (B^i)	
Scan speed SS (C^i)	
Scenario II	Photoinitiator × LP ($A^{ii} \times B^{ii}$)
Photoinitiator (A^{ii})	
Laser power LP (B^{ii})	
Scan speed SS (C^{ii})	
Scenario III	Crosslinker × LP ($A^{iii} \times B^{iii}$)
Crosslinker (A^{iii})	
Laser power LP (B^{iii})	
Scan speed SS (C^{iii})	

Finally, the FFA for scenario III (effect of the crosslinker, Fig. 5c) demonstrated a significant, ordinal two-way interaction between the crosslinker and LP ($A^{iii} \times B^{iii}$): high LP values resulted in higher E_R values for all three crosslinkers. However, the combined effect of PETA as a crosslinker and high LP levels resulted in the highest E_R values. BPAEDA results in intermediate E_R values, which are strongly dependent on the LP. PEGDA 700 showed significantly moduli one order of magnitude lower than for the other two crosslinkers, which were affected by the LP considerably.

Conclusions

Navigating the extensive parameter space in MPLP is challenging but essential for accurately tailoring the structures final properties and unlocking its full potential for targeted applications. In this study, the proposed nano-FFA approach has been successfully applied to elucidate interactions between ink composition and printing parameters in MPLP. By systematically designing and analyzing three different scenarios, we have identified the most significant interacting factors that influence the material properties: Table 1 provides an overview.

Notably, the interaction between ink composition (factor A) and LP (factor B) was shown to be significant across all scenarios. Below two key findings based on the studied scenarios:

I. Higher photoinitiator concentrations allows for more consistent mechanical properties across the studied LP and SS pairs.

II. Crosslinkers leading to 'softer' structures, such as PEGDA 700 and BPAEDA, allow for a greater tunability of the mechanical properties.

In conclusion, this study highlights the power of statistical data analysis, specifically FFA, in understanding the relationships between ink design, processing parameters, and material properties in MPLP. By employing systematic experimental design and FFA, we provide a practical framework for designing materials tailored to specific applications. We envision that this nano-FFA approach will be extended to further ink compositions and processing parameters, making it a versatile tool in advanced material design for high resolution 3D printing.

Experimental section

Materials

Pentaerythritol triacrylate (PETA) was purchased from polysciences. 7-Diethylamino-3-thenoylcoumarin (97%, DETC, Combi Blocks Inc.), phenylbis(2,4,6-trimethylbenzoyl)phosphine oxide (97%, BAPO), poly(ethylene glycol) diacrylate (average Mn 700, PEGDA 700) and bisphenol A ethoxylate diacrylate (average Mn 468, BPAEDA) were purchased from Sigma Aldrich. Acetone (technical grade) and isopropanol (HPLC grade) were purchased from Fisher Scientific. Toluene (≥99.7%) was purchased from Honeywell. 3-(Trimethoxysilyl) propyl acrylate (98%) was purchased from BLDpharm. Sylgard 184 PDMS (Dow Chemical) was purchased from Farnell and used for the preparation of polydimethylsiloxane (PDMS) molds for printing. All materials were used as received without further purification unless indicated. The photoinitiator (2*E*,6*E*)-2,6-Bis (4-(dibutylamino)benzylidene)-4-methylcyclohexanone (BBK) was prepared as reported previously.[39] Further, all chemicals and samples were stored and handled under yellow light conditions.

Methods

Ink preparation. The desired photoinitiator was given into a previously tared 5 mL amber vial. Then, 3 g of the crosslinker of choice were added. The mixture was sonicated for 1 h and then sirred overnight at 250 rpm to ensure homogeneity. All inks were used within one day of preparation.

Silanization of the coverslips was performed before MPLP to improve adhesion to the glass surface. Glass coverslips (22 × 22 mm, 170 μm thickness) were washed with isopropanol and acetone and dried under pressurized N_2. Next, the surface was cleaned and activated for at least 1.5 h by plasma treatment. The coverslips were then immersed in a 4×10^{-3} M solution of 3-(trimethoxysilyl)propyl acrylate in toluene overnight. Finally, after washing twice in toluene and once in acetone, the silanized glass slides were used for MPLP.

PDMS molds were prepared as recommended in the data sheet:[59] The liquid pre-polymer base and a crosslinking curing agent were mixed thoroughly in a 10 : 1 ratio. After mixing, the PDMS was degassed under vacuum until it did not show any more air bubbles. Then 7 g were cast into round Petri dishes (92 × 16 mmstructures) and cured under ambient conditions for at least 72 h. Once cured, rectangular molds were cut off the PDMS sheet with the help of a scalpel (10 × 10 mm outside, 5 × 5 mm inner cavity).

Multiphoton 3D laser printing was performed on the commercially available setup Photonic Professional GT2 (Nanoscribe GmbH & Co. KG) in oil immersion configuration with a femtosecond laser (λ = 780 nm) focused through a 63× oil objective (NA = 1.4; WD = 190 μm; Zeiss). The instrument has a maximum output of 50 mW. The printing GWL files for

 This journal is © The Royal Society of Chemistry 2025

Open Access Article. Published on 29 October 2025. Downloaded on 5/13/2026 5:31:44 PM. This article is licensed under a Creative Commons Attribution 3.0 Unported Licence.

3D structure fabrication were generated from STL files of the desired geometries with the help of the Describe software (Nanoscribe). Slicing and hatching were both set to 300 nm. Silanized cover slides were attached by tape onto a commercial sample holder (Nanoscribe) for oil immersion mode. Immersion oil was added on the unfunctionalized slide surface, and the ink on the functionalized one to ensure good adhesion of the 3D printed microstructures. To maintain the environmental conditions of the ink as stable and reproducible as possible, the ink was loaded into a PDMS mold previously prepared and covered with a circular coverslip during printing. After printing, the PDMS mold and uncured ink were removed. The developing procedure includes developing 5 min in 1 : 1 acetone/isopropanol mixture followed by drying. MPLP and the entire sample preparation and development were performed under yellow light conditions.

Scanning electron microscopy (SEM) was performed using a field-emission scanning electron microscope (Ultra 55, Carl Zeiss Microscopy) at a primary electron energy of 3 keV. Prior to imaging, the 3D printed structures were sputter coating the sample with a 12 nm layer of Pt : Pd (80/20). Image tiles were exported as TIFF files. To create an overview image of the dose test performed for each ink, single tiles were stitched with the Grid/Collection Stitching plugin with a custom ImageJ macro using the Software FIJI.[60]

Nanoindentation was performed at room temperature on 60 (d) × 15 (h) μm 3D printed cylindrical micropillars using a Bruker Hysitron TI 980 Nanoindenter equipped with a BioXR transducer. A 10.26 μm radius conospherical tip made of diamond was employed for this study. Prior to the measurements, the indentation tip was calibrated against air. All indents were performed in displacement control. An adapted displacement profile based on previous work[61] has been employed. The data were then analyzed using the Origin App "Soft Matter Analysis" which belongs to the Bruker's Tribo iQ suite of the technique-specific software applications and E_R was calculated from the recorded load-displacement curves.[62] All measurements were performed in triplicates, and the results are shown as mean ± SD.

Vibrational spectroscopy: Fourier-transform infrared spectroscopy was conducted in the case of the unpolymerized BPAEDA and PETA reference species ("liquid") on a Jasco FT/IR-4600 FT-IR spectrometer in ATR mode with a resolution of 1 cm^{-1} and 128 scans. In the case of the 2PLP 3D printed microstructures ("solid" species), infrared spectra of 60 (d) × 15 (h) μm 3D printed cylindrical micropillars were taken using Bruker LUMOS II FTIR microscope in ATR mode with a resolution of 4 cm^{-1} and 128 scans using a LN-MCT Mid detector (liquid N_2 cooled). In the case of the samples prepared using PEGDA 700 as crosslinker, as well as the unpolymerized PEGDA 700 reference, Raman spectroscopy was conducted with a confocal Raman spectrometer (Renishaw InVia Reflex) in backscattering configuration equipped with a 532 nm laser and a 50× long working distance objective (Olympus, NA = 0.5). A calibration with a silicon wafer at 520.6 cm^{-1} was performed prior to each measurement. Each spectrum was recorded with 20 s of bleaching time, 5 s of integration time, 10 accumulations, and laser power of 100%. Further information regarding data processing is provided in the SI.

Full factorial analysis (FFA). Datasets were analyzed using SPSS and R software packages (see Data availability) using a univariate general linear model. A 3^3 replicated full factorial design with 3 replicates per cell was employed. As mentioned earlier, we adopt a conservative approach in analyzing the results. Thus, the hypothesis tests were conducted at the significance level of $\alpha = 0.005$.[58] Consequently, the null hypotheses were rejected if the obtained p-value is less than the predetermined threshold value of α, *i.e.* if $p < 0.005$. The GFD package in R was used to complement the corresponding F tests in the ANOVA analysis with the Wald test. Only when both analyses agree on their conclusions, factors and their interactions were considered statistically significant. Further details are provided in the SI.

Author contributions

The manuscript was written through contributions of all authors. All authors have given approval to the final version of the manuscript.

Conflicts of interest

There are no conflicts to declare.

Data availability

The data supporting this article have been included as part of the supplementary information (SI) and include information of the full factorial analysis, IR data processing, ink formulation specifications, and additional SEM images. Supplementary information is available. See DOI: https://doi.org/10.1039/d5nr02899j.

Raw data and code for this article are openly available in heiDATA, the Open Research Data institutional repository for Heidelberg University at https://doi.org/10.11588/DATA/5G4P3G.

Acknowledgements

E. B. acknowledges the funding from the Deutsche Forschungsgemeinschaft (DFG, German Research Foundation) *via* the Excellence Cluster "3D Matter Made to Order" (EXC-2082/1-390761711) and the Carl Zeiss Foundation through the "Carl-Zeiss-Foundation-Focus@HEiKA".

The authors thank P. Klee for her assistance during FTIR measurements and J. Lukes for the support during nanoindentation measurements. In addition, the authors want to warmly thank Prof. F. J. V. Polo for the fruitful discussions regarding statistical analysis. The authors thank Prof. Zaumseil for

access to the confocal Raman spectrometer and S. Lindenthal for training on the instrument. In addition, R. Schröder, I. Wagner and R. Curticean are thanked for the access and training at the electron microscopy facilities. The authors gratefully acknowledge the data storage service SDS@hd supported by the Ministry of Science, Research and the Arts Baden-Württemberg (MWK) and the German Research Foundation (DFG) through grant INST 35/1503-1 FUGG.

Open Access Article. Published on 29 October 2025. Downloaded on 5/13/2026 5:31:44 PM. This article is licensed under a Creative Commons Attribution 3.0 Unported Licence.

References

1 S. C. Ligon, R. Liska, J. Stampfl, M. Gurr and R. Mülhaupt, *Chem. Rev.*, 2017, **117**, 10212–10290.
2 S. Kawata, H. B. Sun, T. Tanaka and K. Takada, *Nature*, 2001, **412**, 697–698.
3 C. Greant, B. van Durme, J. van Hoorick and S. van Vlierberghe, *Adv. Funct. Mater.*, 2023, **33**, 2212641.
4 C. N. LaFratta, J. T. Fourkas, T. Baldacchini and R. A. Farrer, *Angew. Chem., Int. Ed.*, 2007, **46**, 6238–6258.
5 M. T. Raimondi, S. M. Eaton, M. M. Nava, M. Laganà, G. Cerullo and R. Osellame, *J. Appl. Biomater. Funct. Mater.*, 2012, **10**, 55–65.
6 G. von Freymann, A. Ledermann, M. Thiel, I. Staude, S. Essig, K. Busch and M. Wegener, *Adv. Funct. Mater.*, 2010, **20**, 1038–1052.
7 P. Mainik, C. A. Spiegel and E. Blasco, *Adv. Mater.*, 2024, **36**, 2310100.
8 S.-F. Liu, Z.-W. Hou, L. Lin, Z. Li and H.-B. Sun, *Adv. Funct. Mater.*, 2023, **33**, 2211280.
9 S. van Kesteren, X. Shen, M. Aldeghi and L. Isa, *Adv. Mater.*, 2023, **35**, e2207101.
10 E. Yarali, M. Klimopoulou, K. David, P. E. Boukany, U. Staufer, L. E. Fratila-Apachitei, A. A. Zadpoor, A. Accardo and M. J. Mirzaali, *Acta Biomater.*, 2024, **177**, 228–242.
11 A. Maggi, H. Li and J. R. Greer, *Acta Biomater.*, 2017, **63**, 294–305.
12 B. Yi, Q. Xu and W. Liu, *Bioact. Mater.*, 2022, **15**, 82–102.
13 J. Bauer, A. Guell Izard, Y. Zhang, T. Baldacchini and L. Valdevit, *Adv. Mater. Technol.*, 2019, **4**, 1900146.
14 J. Li, A. Accardo and S. Liu, *J. Appl. Mech.*, 2024, **91**, 011002.
15 T. Koch, W. Zhang, T. T. Tran, Y. Wang, A. Mikitisin, J. Puchhammer, J. R. Greer, A. Ovsianikov, F. Chalupa-Gantner and M. Lunzer, *Adv. Mater.*, 2024, **36**, e2308497.
16 N. Rohbeck, R. Ramachandramoorthy, D. Casari, P. Schürch, T. E. Edwards, L. Schilinsky, L. Philippe, J. Schwiedrzik and J. Michler, *Mater. Des.*, 2020, **195**, 108977.
17 C. Y. Khripin, C. J. Brinker and B. Kaehr, *Soft Matter*, 2010, **6**, 2842.
18 R. Garcia, *Chem. Soc. Rev.*, 2020, **49**, 5850–5884.
19 S. E. Arevalo, D. M. Ebenstein and L. A. Pruitt, *J. Mech. Behav. Biomed. Mater.*, 2022, **134**, 105384.
20 S. O. Catt, C. Vazquez-Martel and E. Blasco, *Mol. Syst. Des. Eng.*, 2025, **10**, 176–183.
21 K. Cicha, T. Koch, J. Torgersen, Z. Li, R. Liska and J. Stampfl, *J. Appl. Phys.*, 2012, **112**, 094906.
22 J. S. Oakdale, J. Ye, W. L. Smith and J. Biener, *Opt. Express*, 2016, **24**, 27077–27086.
23 L. J. Jiang, Y. S. Zhou, W. Xiong, Y. Gao, X. Huang, L. Jiang, T. Baldacchini, J.-F. Silvain and Y. F. Lu, *Opt. Lett.*, 2014, **39**, 3034–3037.
24 X. Gou, M. Zheng, Y. Zhao, X. Dong, F. Jin, J. Xing and X. Duan, *Appl. Surf. Sci.*, 2017, **416**, 273–280.
25 E. D. Lemma, F. Rizzi, T. Dattoma, B. Spagnolo, L. Sileo, A. Qualtieri, M. de Vittorio and F. Pisanello, *IEEE Trans. Nanotechnol.*, 2016, **16**, 23–31.
26 J. Bauer, A. G. Izard, Y. Zhang, T. Baldacchini and L. Valdevit, *Opt. Express*, 2020, **28**, 20362–20371.
27 M. Belqat, X. Wu, L. P. C. Gomez, J.-P. Malval, S. Dominici, B. Leuschel, A. Spangenberg and K. Mougin, *Addit. Manuf.*, 2021, **47**, 102232.
28 M. Diamantopoulou, N. Karathanasopoulos and D. Mohr, *Addit. Manuf.*, 2021, **47**, 102266.
29 Q. Hu, G. A. Rance, G. F. Trindade, D. Pervan, L. Jiang, A. Foerster, L. Turyanska, C. Tuck, D. J. Irvine, R. Hague and R. D. Wildman, *Addit. Manuf.*, 2022, **51**, 102575.
30 K. S. Worthington, L. A. Wiley, E. E. Kaalberg, M. M. Collins, R. F. Mullins, E. M. Stone and B. A. Tucker, *Acta Biomater.*, 2017, **55**, 385–395.
31 F. Matheuse, K. Vanmol, J. van Erps, W. de Malsche, H. Ottevaere and G. Desmet, *J. Chromatogr. A*, 2022, **1663**, 462763.
32 A. Isaakidou, M. Ganjian, V. Moosabeiki, M. A. Leeflang, M. N. Goushki, P. E. Boukany, M. Wątroba, A. Groetsch, J. Schwiedrzik, M. J. Mirzaali, I. Apachitei, L. E. Fratila-Apachitei and A. A. Zadpoor, *Adv. Eng. Mater.*, 2025, e202500977.
33 R. Carlson and J. E. Carlson, in *Comprehensive Chemometrics*, ed. R. Tauler, B. Walczak and S. D. Brown, Elsevier, Burlington, 2009, pp. 301–344.
34 B. Benedetti, V. Caponigro and F. Ardini, *Crit. Rev. Anal. Chem.*, 2022, **52**, 1015–1028.
35 D. C. Montgomery, *Design and analysis of experiments*, Wiley, Hoboken, NJ, 2020.
36 R. Leardi, in *Chemometrics in food chemistry*, ed. F. Marini, Elsevier, Amsterdam, 1st edn, 2013, pp. 9–53.
37 J. Fischer, J. B. Mueller, J. Kaschke, T. J. A. Wolf, A.-N. Unterreiner and M. Wegener, *Opt. Express*, 2013, **21**, 26244–26260.
38 J. Fischer, J. B. Mueller, A. S. Quick, J. Kaschke, C. Barner-Kowollik and M. Wegener, *Adv. Opt. Mater.*, 2015, **3**, 221–232.
39 P. Kiefer, V. Hahn, M. Nardi, L. Yang, E. Blasco, C. Barner-Kowollik and M. Wegener, *Adv. Opt. Mater.*, 2020, **8**, 2000895.
40 P. Somers, Z. Liang, T. Chi, J. E. Johnson, L. Pan, B. W. Boudouris and X. Xu, *Nanophotonics*, 2023, **12**, 1571–1580.
41 L. Yang, A. Münchinger, M. Kadic, V. Hahn, F. Mayer, E. Blasco, C. Barner-Kowollik and M. Wegener, *Adv. Opt. Mater.*, 2019, **7**, 1901040.

 This journal is © The Royal Society of Chemistry 2025

Open Access Article. Published on 29 October 2025. Downloaded on 5/13/2026 5:31:44 PM.
This article is licensed under a Creative Commons Attribution 3.0 Unported Licence.

42 C. Barner-Kowollik, M. Bastmeyer, E. Blasco, G. Delaittre, P. Müller, B. Richter and M. Wegener, *Angew. Chem., Int. Ed.*, 2017, **56**, 15828–15845.
43 J. Fischer and M. Wegener, *Laser Photonics Rev.*, 2013, **7**, 22–44.
44 Q. Hu, X.-Z. Sun, C. D. J. Parmenter, M. W. Fay, E. F. Smith, G. A. Rance, Y. He, F. Zhang, Y. Liu, D. Irvine, C. Tuck, R. Hague and R. Wildman, *Sci. Rep.*, 2017, **7**, 17150.
45 F. Zhang, Q. Hu, A. Castañon, Y. He, Y. Liu, B. T. Paul, C. J. Tuck, R. Hague and R. D. Wildman, *Addit. Manuf.*, 2017, **16**, 206–212.
46 J. B. Mueller, J. Fischer, F. Mayer, M. Kadic and M. Wegener, *Adv. Mater.*, 2014, **26**, 6566–6571.
47 J. B. Mueller, J. Fischer, Y. J. Mange, T. Nann and M. Wegener, *Appl. Phys. Lett.*, 2013, **103**, 123107.
48 A. Mauri, P. Kiefer, P. Neidinger, T. Messer, N. M. Bojanowski, L. Yang, S. Walden, A.-N. Unterreiner, C. Barner-Kowollik, M. Wegener, W. Wenzel and M. Kozlowska, *Chem. Sci.*, 2024, **15**, 12695–12709.
49 J. E. Johnson, I. R. Jamil, L. Pan, G. Lin and X. Xu, *Light: Sci. Appl.*, 2025, **14**, 56.
50 P. Somers, Z. Liang, J. E. Johnson, B. W. Boudouris, L. Pan and X. Xu, *Light: Sci. Appl.*, 2021, **10**, 199.
51 A. Mauri, P. Kiefer, W. Wenzel and M. Kozlowska, *Macromol. Rapid Commun.*, 2025, 2500231.
52 Y. Bao, *Macromol. Rapid Commun.*, 2022, **43**, 2200202.
53 F. Kröger, R. Eichelmann, G. Sauter, A. Pollien, P. Tegeder, L. H. Gade and E. Blasco, *RSC Appl. Polym.*, 2024, **2**, 847–856.
54 T. Zandrini, N. Liaros, L. J. Jiang, Y. F. Lu, J. T. Fourkas, R. Osellame and T. Baldacchini, *Opt. Mater. Express*, 2019, **9**, 2601.
55 R. Anastasio, R. Cardinaels, G. W. M. Peters and L. C. A. van Breemen, *J. Appl. Polym. Sci.*, 2020, **137**, 48498.
56 K. McAvoy, D. Jones and R. R. S. Thakur, *Pharm. Res.*, 2018, **35**, 36.
57 J. P. Mazzoccoli, D. L. Feke, H. Baskaran and P. N. Pintauro, *J. Biomed. Mater. Res., Part A*, 2010, **93**, 558–566.
58 D. J. Benjamin and J. O. Berger, *Am. Stat.*, 2019, **73**, 186–191.
59 The Dow Chemical Company, Technical Data Sheet Sylgard 184, https://www.dow.com/en-us/document-viewer.html?docPath=/content/dam/dcc/documents/11/11-3184-01-sylgard-184-elastomer.pdf (accessed 17 October 2025).
60 S. Preibisch, S. Saalfeld and P. Tomancak, *Bioinformatics*, 2009, **25**, 1463–1465.
61 O. Eivgi, C. Vazquez-Martel, J. Lukeš and E. Blasco, *Small Methods*, 2025, e2500432.
62 G. Huang and H. Lu, *Mech. Time-Depend. Mater.*, 2006, **10**, 229–243.